



Method for Minefields Mapping by Imagery from Unmanned Aerial Vehicle

M. O. Popov^{1*}, S. A. Stankevich¹, S. P. Mosov², O. V. Titarenko¹,
S. S. Dugin¹, S. I. Golubov¹ and A. A. Andreiev¹

¹ *Scientific Centre for Aerospace Research of the National Academy
of Sciences of Ukraine, Kyiv, Ukraine*

² *Institute of Public Administration and Research in Civil Protection,
SES of Ukraine, Kyiv, Ukraine*

The manuscript was received on 16 March 2022 and was accepted
after revision for publication as research paper on 7 September 2022.

Abstract:

The paper proposes a method for minefields mapping by the centimeter resolution imagery from a copter-type unmanned aerial vehicle (UAV) which is equipped with multispectral camera and thermal infrared camera. The research methodology is the probability fusion by each sensor and the subsequent decision making on the landmine presence/absence. Models for the landmine detection in multispectral and thermal images are considered. The training sample structuration is proposed for the landmine detection reliability enhancement. The local temperature anomalies of landmine size are allocated by sliding window scanning the thermal image. The experimental performance of actual landmines detection at a special test site in Ukraine is described. The probability of correct landmine detection was 0.92 while with a false alarm probability it was 0.45.

Keywords:

landmine detection, minefield mapping, multispectral camera, probability fusion, thermal infrared camera, uncertainty level, unmanned aerial vehicle

1 Introduction

As a rule, any war or military conflict is inextricably linked with the mining of territories. According to the Geneva International Centre for Humanitarian Demining, as of January 2021, more than 60 countries have faced numerous cases of destructions by undetected anti-personnel landmines [1]. Ukraine is among these countries.

The landmine clearance challenge is in the focus of attention of high-profile international and national organizations; experts from many countries of the world are working on its solution. A large number of different methods and systems for landmine clearance have been developed – see, for example, [2, 3], which can significantly increase the demining efficiency, but the problem of deminer's personal safety remains pressing. This problem can be solved essentially by ground-based robotic

systems, but their performance is not yet high enough, and their use is possible only in limited landscape conditions.

Therefore, a remote approach to the landmines, unexploded and abandoned ordnances detection by analyzing aerial imagery of terrain was proposed in the early 2000s [4]. A number of remote mine detection systems were developed, in particular, ASTAMIDS and AMDAS systems [5], with imaging sensors installed on piloted helicopters. However, as a rule, the copter-type unmanned aerial vehicles (UAVs) are used as a mobile platform for onboard sensors in the last decade of engineering developments [6-9].

Multispectral, hyperspectral, thermal infrared cameras, radar systems, etc., are used from UAVs to acquire images of the inspected area [10-12].

The specific composition of the onboard payload is aimed to ensure the maximum probability of landmine detection, while satisfying certain restrictions on cost, technical complexity, duration of continuous operation, jamming resistance and others.

Further, the paper is organized as follows. Section 2 defines the research objective. The study methodology is described in Section 3. The constructive result of the work – the method for minefields mapping – is presented in section 4. The experimental results of the developed method testing are given in section 5. Section 6 discusses the results obtained, and section 7 briefly summarizes the research outputs.

2 Research Objective

The research objective is to propose and substantiate an efficient method for minefields mapping by terrain imaging from a mobile light airborne platform.

A common copter-type UAV was chosen as such a platform. Taking into account \bar{M} the cost and technical complexity limitations, it was determined that the UAV's onboard sensors set for the terrain imaging consists of a multispectral (MS) camera, a thermal infrared (TIR) camera and a conventional color digital (CD) camera.

3 Methodology

The study is based on the following methodological considerations [13]:

- data on the physical properties of the land surface contain indicative information about the landmine presence/absence within the corresponding area,
- the data on the physical properties of land surface is obtained by imaging sensors installed on a mobile airborne platform,
- the decision on the landmine presence/absence is made on the basis of a comprehensive analysis of the data obtained by various onboard sensors.

Let us consider that our interest is a land surface element of a small area that may pose a threat. Then, we will assume that if there is a mine in this element ($M =$ “land mine”), then case A takes place ($A =$ “presence of a threat”), and vice versa, case A does not occur (i.e. \bar{A}), if there is no mine (i.e. \bar{M}). Then the alarm occurrence probability due to the buried landmine is calculated as

$$p(A) = p(A|M)p(M) + p(A|\bar{M})p(\bar{M}) \quad (1)$$

where $p(M)$ is a landmine occurrence probability, $p(A|M)$ is a conditional probability of the threat, and $p(A|\bar{M})$ is a probability of false alarm.

Eq. (1) shows that the threat probability is determined primarily by information about the landmine presence/absence. It is assumed that such information can be ob-

tained by the onboard sensor. However, it should be noted that for a number of reasons (both natural and technical), it is generally not possible to ensure a high probability of landmine detection with any single sensor. In this regard, it becomes clear that there is a need to involve several different sensors simultaneously for landmine detection [6].

Combining the data received by several sensors operating in parallel increases the landmine detection likelihood, but, unfortunately, at the same time, it increases the number of false alarms [14]. An increase in the number of false alarms puts an additional strain on deminer and can significantly extend the time required to perform the landmine clearance task. One efficient way to reduce the number of false alarms is to engage modern algorithms for signal classification [15].

Suppose that N sensors are used for a minefield mapping. All of them generate a terrain scene image of the same ground sample distance (GSD) but in different spectral bands. If all these images have the same raster structure and are pixel-wise co-registered with each other, then this makes it possible to obtain a description of the GSD-size land surface element as an N -dimensional pixel signal

$$S = \{s^{(1)}, \dots, s^{(n)}, \dots, s^{(N)}\} \quad (2)$$

where $s^{(n)}$ is the level of signal generated by the n -th sensor.

According to the adopted methodological considerations, the landmine presence can affect the land surface properties. This element (pixel) of the digital image may contain certain information about the landmine presence. Thus, according to the known pixel signal, it is possible to provide some estimate for the conditional probability of the landmine presence inside the land surface element, which is represented by the current pixel.

And then, the aim is to make an appropriate decision on the landmine presence or absence within the corresponding terrain element using this estimate in accordance with the defined rule.

4 Method

Based on the above methodological considerations, a new remote method for minefield map acquisition has been developed. The method consists of the following procedures (Fig. 1):

- aerial imaging mission planning,
- aerial imaging performing,
- pre-processing of aerial imagery,
- production of digital image mosaics,
- smoothing of digital image mosaics,
- pixel-wise classification of digital image mosaics,
- decision making,
- documenting.

Below, each procedure is described consistently and in detail.

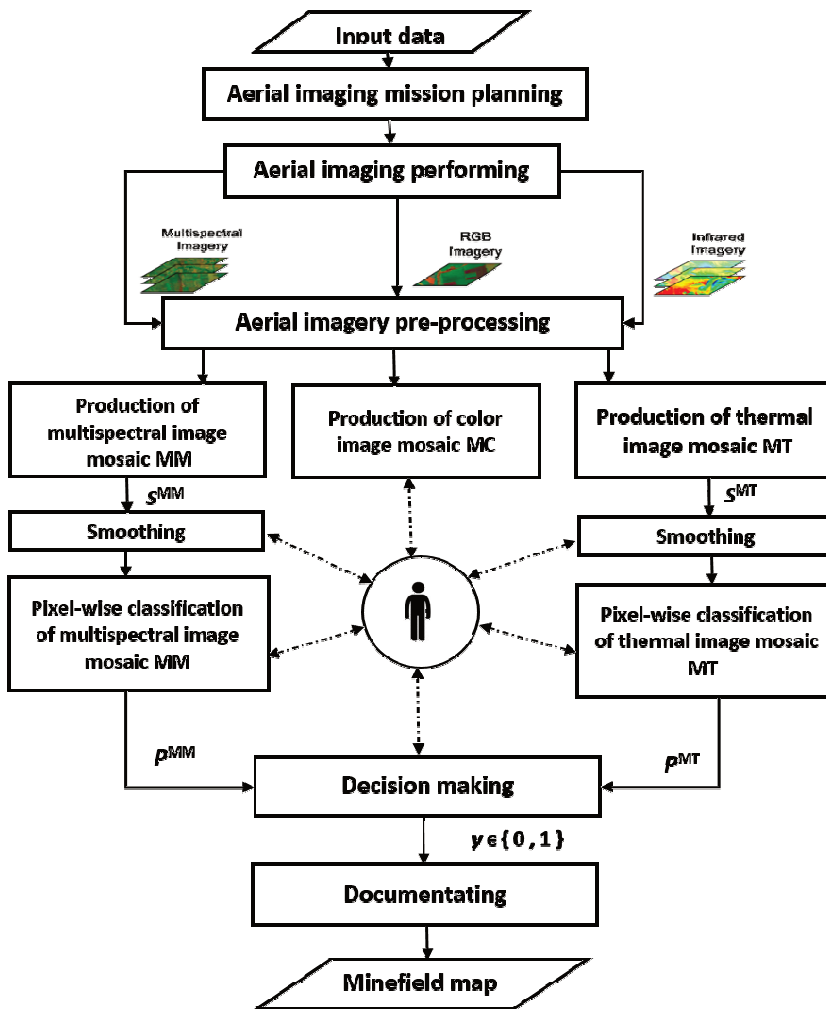


Fig. 1 Flowchart of the method for minefields mapping

4.1 Aerial Imaging Mission Planning

It is performed based on current instructional and methodological documents, taking into account information on the territory and specifications of the equipment used and considering the customer's operation requests. For example, the customer's requests may include the maximum allowable time for the task, the accuracy of the output data product, the required level of information protection, etc.

The information on the territory should include:

- coordinate allocation of the area of interest,
- data on the terrain configuration (soil type, vegetation cover, possible artificial objects, etc.),
- information about the expected landmines category (anti-personnel, anti-tank).

The following must be known about the equipment used:

- flight and technical specifications of UAV,
- technical specifications of onboard sensors,
- onboard storage capacity,
- radio link parameters, etc.

The task of aerial imaging mission planning is to establish the route, to calculate UAV flight altitude and the frame acquisition frequency over the territory.

The route is established based on the requirements of full coverage of the entire area of the minefield and the provision of a given transverse overlap (usually 40-60 %).

The altitude of the UAV is calculated based on the necessary number of pixels within a single landmine image – at least 50-70 pixels per landmine segment.

The frequency of the frame-by-frame imaging of the territory should provide a required value of the longitudinal overlap (usually 30-40 %) of the image frames formed by the onboard sensor.

4.2 Aerial Imaging Performing

A typical UAV flight route while imaging an area of interest is shown in Fig. 2. The flight and control parameters of the imaging process are programmable, with particular attention to the endurance of the pre-estimated flight altitude and camera operating synchronization.

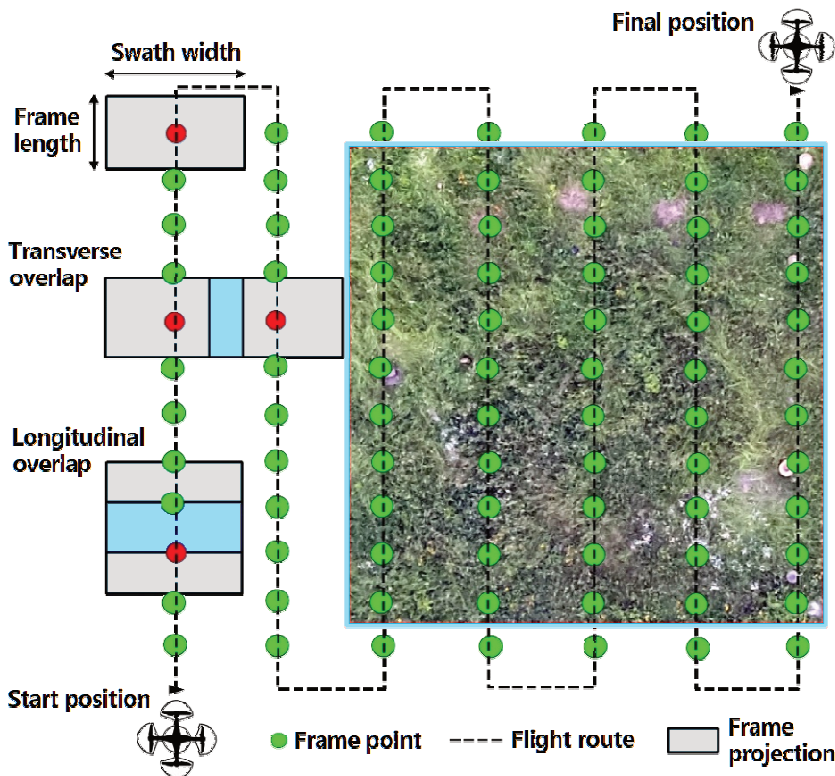


Fig. 2 A typical UAV flight route while imaging an area of interest [16, adapted]

Each element of the surveyed area is simultaneously taken on three digital images: multispectral, thermal infrared, and conventional in natural colors.

A multispectral image consists of several separate band images (the number of bands denoted as the L), each of which is formed in a specific optical spectrum. A thermal infrared image registers the land surface temperature values in each pixel. The color image contains terrain information in the unified RGB (red, green, blue) view.

Depending on the requirements and available technical capabilities, the full amount of data registered by onboard sensors can be recorded to the onboard storage or transmitted to the ground receiving and processing station.

4.3 Aerial Imagery Pre-Processing

All acquired images of the territory require pre-processing. Pre-processing operations are radiometric and spatial correction, raster structure regularization, different images co-registering, and geo-referencing. In some cases, noise and distortions filtering is performed over the “raw” images.

4.4 Production of Digital Image Mosaics

Each sensor’s full package of digital images is assembled into a joint image mosaic. One of the well-known photogrammetric applications can be used for this, for example, proprietary Pix4D Mapper, Agisoft Metashape, Digital Professional, or free open source ones, such as OpenDroneMap [17]. As a rule, the service deliveries of most branded drones include software packages for aerial imaging mission planning, which often include photogrammetric modules for the image mosaic compilation.

Thus, the following data are obtained:

- multispectral image mosaic MM (consists of L layers, corresponding with the number of band images),
- thermal infrared image mosaic MT . This one is single-layered,
- color image mosaic MC with RGB images.

All image mosaics have the same number of pixels (we will denote this number as K), and the corresponding pixels of image mosaics are numbered the same.

Let us consider how MM and MT image mosaics are processed and analyzed to detect landmines and form a minefield map.

4.5 Smoothing Digital Image Mosaics

The size of the terrain element GSD is gnomonically projected to one pixel of any band image. If the GSD size is about 1-3 cm, then this is much smaller than the landmine segment’s diameter. To reduce the random variability of pixel signals per landmine, the smoothing of the image mosaics is required. This operation is performed in a cycle with an isotropic sliding round window. The radius of the sliding window in pixels is calculated as

$$r = \sqrt{\frac{G}{\pi}} \quad (3)$$

where G is the number of pixels in the landmine image segment.

After smoothing operations accomplishment, the two datasets are formed. The first one consists of pixel signals of the *MM* image mosaic; the signal of any k -th pixel of this image mosaic has the vector form:

$$\mathbf{S}^{MM}(k) = \{\tilde{s}_1^{MM}(k), \dots, \tilde{s}_l^{MM}(k), \dots, \tilde{s}_L^{MM}(k)\}, \quad k = 1, 2, \dots, K \quad (4)$$

where $\tilde{s}_l^{MM}(k)$ is the level of the smoothed signal in the k -th pixel of the l -th layer of the image mosaic.

The second dataset is a sequence of pixel signals of the *MT* image mosaic:

$$\mathbf{S}^{MT} = \{\tilde{s}^{MT}(k)\}, \quad k = 1, 2, \dots, K \quad (5)$$

where $\tilde{s}^{MT}(k)$ is the level of the smoothed signal of the k -th pixel of this image mosaic.

The next operation is the pixel-wise classification of *MM* and *MT* image mosaics to detect landmines.

4.6 Pixel-Wise Classification of Digital Image Mosaics

The pixels of the *MM* and *MT* mosaics are classified semi-automatically with the participation of an operator. The operator's contribution includes adjusting the parameters of the classification algorithm, interactive formation of a training sample by visual interpretation of terrain elements using *MC* image mosaics, controlling the algorithm operation and evaluating the classification results.

Pixel-wise classification of *MM* image mosaic. It is carried out by the method of binary logistic regression [18]. It is assumed that any pixel of an image mosaic, depending on its unique signal, can belong to either of two classes. Belonging to the first class means that this pixel reflects a terrain element with a landmine. If the terrain element displayed by this pixel does not contain a landmine, it belongs to the second class. Therefore, the first class pixels will be encoded by $y = 1$ label, and second class pixels – by $y = 0$ label.

The image mosaic *MM* signal (4) determines the class label for each pixel in dataset.

According to the method of binary logistic [19], the probability that the k -th pixel with the $\mathbf{S}^{MM}(k)$ signal belongs to the class $y = 1$, is calculated by the expression:

$$\psi_k = p[\mathbf{S}^{MM}(k) | y_k = 1] = \frac{\exp[\omega_0 + \boldsymbol{\omega}^T \mathbf{S}^{MM}(k)]}{1 + \exp[\omega_0 + \boldsymbol{\omega}^T \mathbf{S}^{MM}(k)]} \quad (6)$$

where ω_0 is a scalar, and $\boldsymbol{\omega}$ is a vector.

If a pixel with an \mathbf{S}^{MM} signal is classified with a probability of $p[\mathbf{S}^{MM}] = p^{MM}$ as indicating the landmine presence, it is obvious that the probability that it is not associated with a mine will be $1 - p^{MM}$.

The ω_0 and $\boldsymbol{\omega}$ parameters in equation (6) are unknown, but they can be restored from the training sample which must include pixels of both classes with a mandatory known y label for each pixel.

Let such a training sample of Q pixels size exists. Then the log-likelihood function (LLF) can be formed [19] as:

$$\text{LLF}(\omega_0, \boldsymbol{\omega}) = \sum_{q=1}^Q \left[(1 - y_q) \ln(1 - \psi_q) + y_q \ln \psi_q \right] \quad (7)$$

The ω_0 and ω parameters can be restored by substituting in the right part of (6) the signal values of the training sample pixels and performing reverse optimization [20].

With restored ω_0 and ω , the equation (6) allows estimating the p^{MM} probability of belonging of any pixel of a multispectral image mosaic to the $y = 1$ class. In other words, it becomes possible to estimate the probability of a landmine presence at the current pixel.

There is a problem with the training sample required in the regression approach to classification. The fact is that the terrain elements with landmine and without it are very similar in their optical and physical parameters. Therefore, the signal values of the pixel-members of both classes intersect to a great degree. In addition, the surveyed area is usually quite “variegated” (there may be plots of open soil, different-type and different-condition grass, sand, stone drops, etc.). Consequently, the ranges of signal values of the pixel-members are, as a rule, non-compact and consist of a set of separate spaced subdomains. This problem is well illustrated by Fig. 3, which shows the distribution of pixel signals of the actual multispectral image with both landmines and background land covers. It is shown in the plane of band reflectance of the first $\rho(B_1)$ – blue – and fifth $\rho(B_5)$ – near-infrared – operating spectral bands of the multispectral camera installed at DJI Phantom 4 MS light quadcopter.

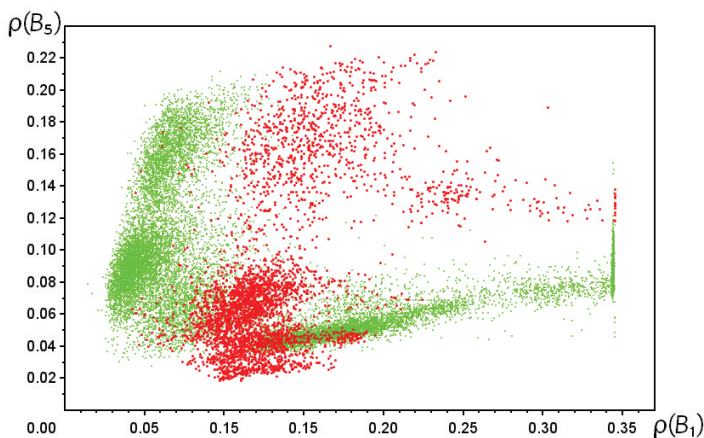


Fig. 3 An example of the pixel signals distribution in actual multispectral image fragments with both landmines (red color) and background land covers (green color)

All foregoing have a negative impact on the classification accuracy. Structuring the training sample helps partially overcome this problem, whereby the algorithm presented in Fig. 4.

Suppose a training sample of pixels is structured, including a subset of first class ($y = 1$) and a subset of second class ($y = 0$). The procedure of iterative clustering by unsupervised classification is applied to the elements of each subset, particularly by the k -means method [21]. The maximum possible number of iterations is constrained by the number of pixels in the subset.

Each iteration consists of three stages. In the first stage, the number of clusters for subset elements is assigned the L . It should be noted that clustering occurs for each subset separately and independently. Each cluster is described by a corresponding centroid.

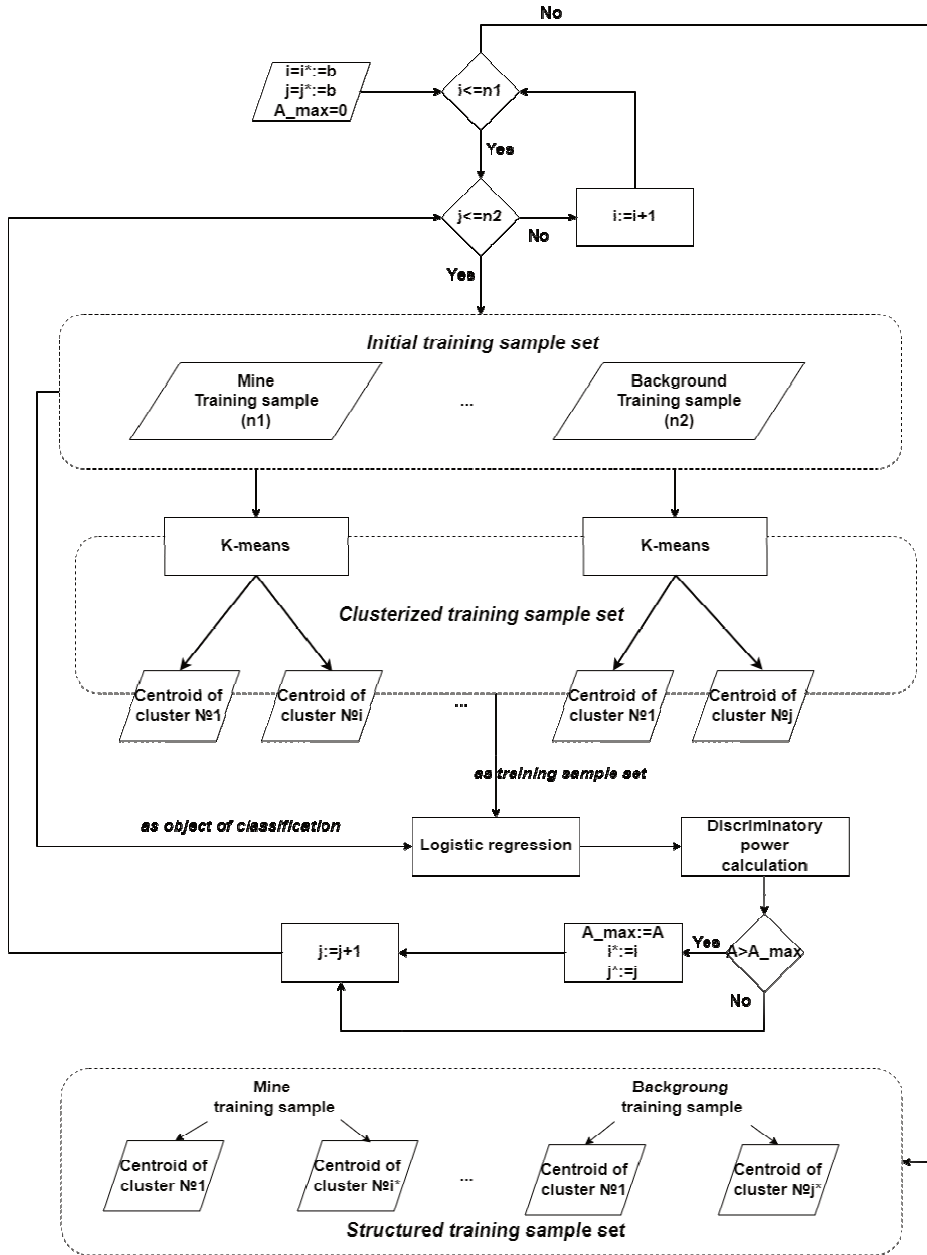


Fig. 4 Flowchart of the training sample structuring

The second stage engages the supervised classification when the training sample elements are used as objects of classification. The set of centroids, which was determined in the previous step, was used as a training sample. Logistic regression was also chosen as the method of supervised classification.

- Based on the results of the classification, the following parameters are calculated:
- number of correct decisions about the presence of the mine TP (true positive),

- number of correct decisions about the absence of the mine TN (true negative),
- number of incorrect decisions about the presence of the mine FP (false positive),
- number of incorrect decisions about the absence of the mine FN (false negative).

In the third stage, the supervised classification results are used to assess the obtained set of centroids in terms of interclass separability. The degree of separability called as DP (discriminatory power) is calculated by the expression [22]:

$$DP = \ln \frac{TP}{FN} + \ln \frac{TN}{FP} \quad (8)$$

A structured set of centroids, which provides the maximum DP value, is selected for further classification. From now on, this set plays the role of a training sample.

Pixel-wise classification of MT image mosaic. In computer analysis of MT image mosaic, the possible landmine locations and the p^{MT} probability of each landmine detection are determined by local temperature anomalies. To ensure an equal area of both anomaly and background, the central sliding window of radius r , calculated with the (3), should be surrounded by a ring with additional radius h :

$$h = r(\sqrt{2} - 1) \quad (9)$$

as shown in Fig. 5.

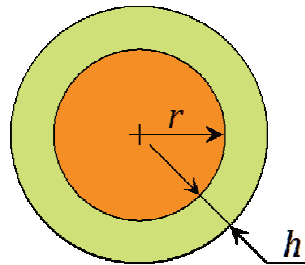


Fig. 5 Sliding window with a surrounding ring

The simplest case of anomaly detection under the condition of normal distributions of temperature values in image segments of the target and the background is described by the probability [23]:

$$p^{MT} = \text{erf} \left(\frac{|T - T_0|}{\sigma_T \sqrt{2}} \right) \quad (10)$$

where T_0 is the mean temperature in the inner window, T is the mean temperature in the surrounding window, σ_T is the standard deviation of the temperature values in both

windows, $\text{erf}(x) = \frac{2}{\sqrt{\pi}} \int_0^x e^{-z^2} dz$ is the integral error function [24].

In the described way, it is possible to move from the point anomalies detection in infrared image to statistical anomalies detection in the thermal mosaic that corresponds to the mine segment size [25]. The operations sequence for thermal anomalies detection is described by the algorithm flowchart presented in Fig. 6.

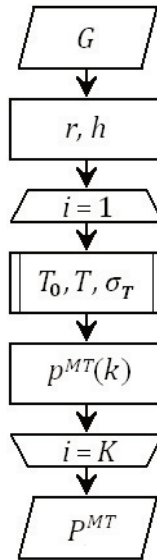


Fig. 6 Algorithm flowchart for mapping thermal anomalies in the MT mosaic

When the expected number of pixels G in the image of the mine is set, then the radii of the scanning windows r and h are calculated by Eqs (3) and (9). Next, the loop scanning of the entire image performs, within which the statistics T_0 , T , σ_T of image fragments inside sliding windows are estimated and the p^{MT} probability values of landmine detection inside current window positions are calculated by Eq. (10).

Obviously, the p^{MT} probability will decrease if the anomaly center diverts from the window center.

The Fig. 6 algorithm applying to the MT image mosaic pixels allows estimating the p^{MT} probability of the landmine presence inside the terrain elements represented by the corresponding pixels.

An example of processing the temperature image obtained from UAV with the FLIR One Pro infrared camera is shown in Fig. 7.

4.7 Decision Making

According to the results of the classification of digital image mosaics, we have two probability distributions: the first one

$$P^{MM} = \{p^{MM}(k)\}, \quad k = 1, 2, \dots, K \quad (11)$$

is for MM image mosaic pixels and another one

$$P^{MT} = \{p^{MT}(k)\}, \quad k = 1, 2, \dots, K \quad (12)$$

is for MT image mosaic pixels.

The decision-making procedure for any k -th pixel ($k = 1, 2, \dots, K$) based on the joint consideration of the probability distributions (11) and (12) includes the following steps.

A combination of probabilities calculated for a pixel by the classification results of both image mosaics is formed. Following the [26], the combination can be written as

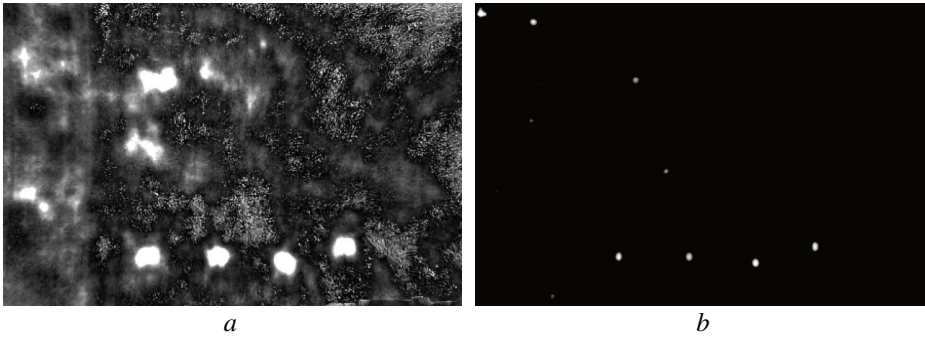


Fig. 7 The result of the landmine detection in the thermal infrared image: a – the input image in the land surface temperature gradations; b – the distribution of the probability of the landmine detection inside a window of an inner radius $r = 32$; lighter color indicates higher probability values

$$\left[(1-u_1) p^{MM}(k) + 0.5u^{MM} \right] \left[(1-u_2) p^{MT}(k) + 0.5u^{MT} \right] \quad (13)$$

where u^{MM} and u^{MT} are statistical uncertainties; $u^{MM}, u^{MT} \in [0; 1]$.

The u^{MM} and u^{MT} parameters are involved in equation (13) to consider the aleatory statistical uncertainty, which occurs because the probability values are obtained in conditions of insufficient amount of input data. The procedure for determining the uncertainty level is described in [27]. The following equation may be written:

$$\left[(1-u_1) p^{MM}(k) + 0.5u^{MM} \right] \left[(1-u_2) p^{MT}(k) + 0.5u^{MT} \right] = \Pi \quad (14)$$

Substituting of (14) the u^{MM} and u^{MT} uncertainties of sensors in the left part, and assuming $p^{MM}(k) = p^{MT}(k) = 0.5$, the Π value can be calculated.

A criterion function is formed:

$$\left[(1-u_1) p^{MM}(k) + 0.5u^{MM} \right] \left[(1-u_2) p^{MT}(k) + 0.5u^{MT} \right] > \Pi \quad (15)$$

The decision rule is: the pixel estimates of the $p^{MM}(k)$ and $p^{MT}(k)$ probabilities are substituted into the Eq. (15). If the inequality holds, it is decided that there is a threat (landmine) in the current terrain element. On the other hand, if condition (15) is not met, a decision is made that there is no threat (no landmine).

Each pixel of the image mosaics passes through step 3, and the decisions are made on the state of the current terrain elements; this information is a basis for the minefield map restoration.

4.8 Documenting

The final data product of the method is a restored map of the minefield, issued according to the adopted regulations [28, 29]. In addition, other information obtained from aerial imagery may be added upon the customer's request.

5 Experimental Results

The testing of the method described above was carried out by detecting dummy landmines and landmine groups that were installed at a test ground site in accordance

with the relevant engineering manuals, in different conditions of burying and camouflage. Several test sites ranging in size from (40 × 30) up to (80 × 60) m were involved in experimental landmine detection. Airborne imagers installed onboard of three light copter-type UAVs by DJI and Parrot were used for landmine detection [30]. Data from the drone's onboard GPS was used for georeferencing the separate frames of aerial imagery.

Airborne imagers set included a P12.4K color digital camera, a P4MS visible and near-infrared multispectral camera and a FLIR One Pro thermal infrared camera. Flight missions planning, including the flight paths generation according to user-defined imaging parameters, as well as the image mosaics compilation from the acquired images was carried out automatically using special-purpose DJI GS Pro software.

The study was conducted in the spring-summer season of 2021 and began with the orthophotomap compilation over the test site using DJI GS Pro aerial survey mission planning software for the selected flight profile (see Fig. 2) [31]. The typical altitude of aerial imaging for landmine detection hovers around 2-10 m, surveillance mosaics were formed from a 50-100 m altitude.

The aerial imaging altitude H was determined under the condition of acquiring a given number of pixels G within the landmine image fragment [32]:

$$H = \frac{l_0 f}{a} \sqrt{\frac{\pi}{4G}} \quad (16)$$

where l_0 is the diameter of the landmine segment on the ground, f is the focal length of the camera optics, a is the photodetector size of the camera's sensor array. Since the f and a parameters are different for multispectral and infrared cameras, the predicted altitudes (16) will also be different. Under the experiment, to ensure the same GSD, multispectral and infrared image sets were acquired by different drones.

Both multispectral and infrared cameras are equipped with a built-in self-calibration subsystems. However, calibration information of DJI multispectral imagery is provided as textual annotation data. Therefore, we were forced to develop special software for the automatic cropping and converting the raw multispectral images into the land surface spectral reflectance distributions.

Detection of different types of landmines in different backgrounds was performed by multispectral and infrared aerial images using specially developed software. Figs 8 and 9 show some examples of test detection of buried and open landmines in multispectral and infrared images, respectively. Left images are multispectral fragments synthesized in pseudo-natural or natural colors; right images are probability distributions (11), (12).

In total, 195 multispectral and 108 infrared aerial images of 14 types of anti-personnel and anti-tank landmines were acquired and processed. A significant part of these aerial images was used as a training sample, also to adjust the algorithm parameters, etc.

Complete sets of images (multispectral + thermal + color) were obtained over 36 test plots. The decision on threatening parcels (with landmines) detection in the images was made by substituting each current pair of probability estimates $\{p^{MM}(k), p^{MT}(k)\}$ into the criterial Eq. (15), which, taking into account the experimentally obtained uncertainty levels $u^{MM} = 0.10$ and $u^{MT} = 0.15$ took the form:

$$\left[0.9 p^{MM}(k) + 0.05 \right] \left[0.85 p^{MT}(k) + 0.075 \right] > II = 0.225 \quad (17)$$

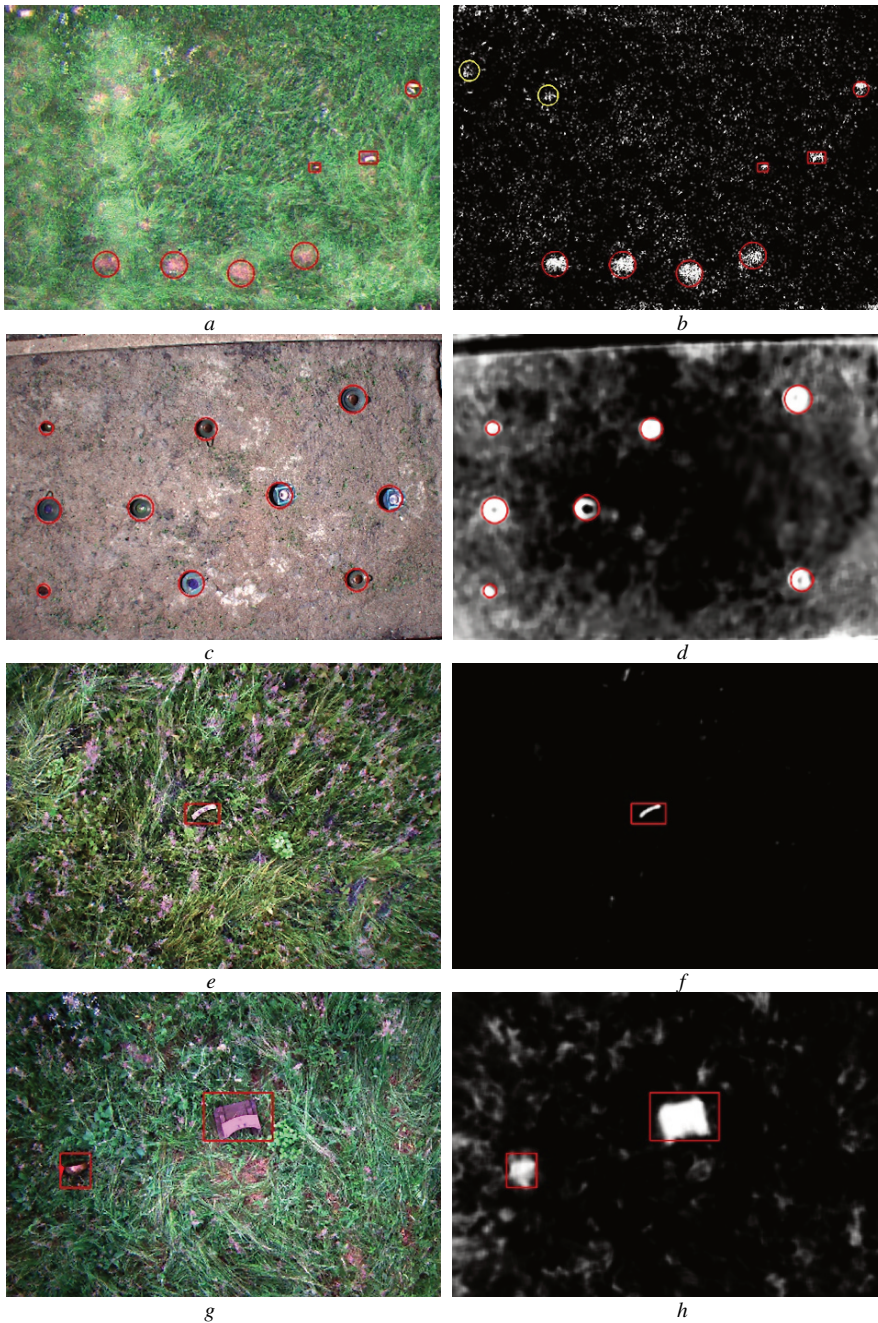


Fig. 8 Examples of landmine detection in multispectral images: a, b – TM-62P3 buried landmine, MON-50, MON-90, MON-100 landmines in the grass; c, d – OZM-72, TM-62M, TM-72 and TM-62P3 open landmines; e, f – MON-50 landmine in the grass; g, h – MON-100 and MON-90 landmines in the grass; a lighter tone indicates the higher probability values; Legend: — – existing (detected) landmine, — – false detection

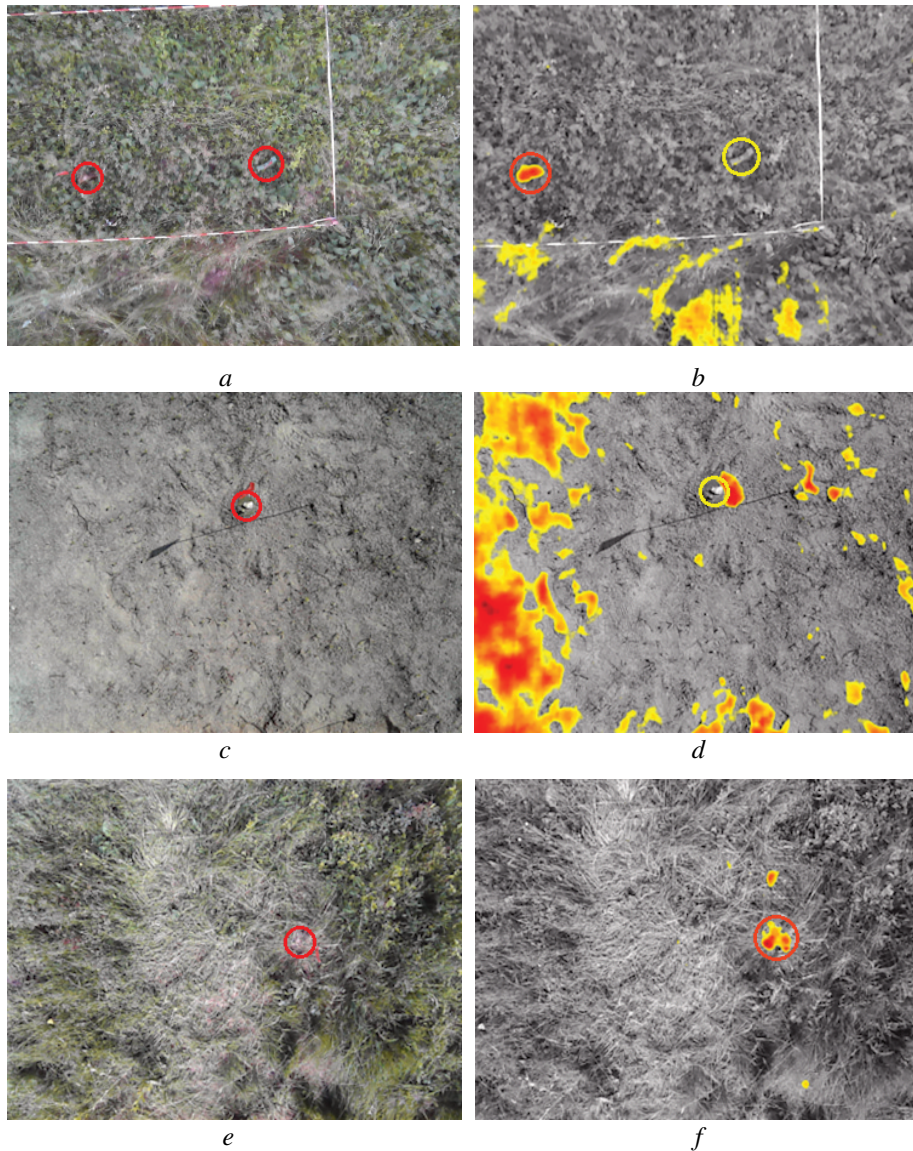


Fig. 9 Examples of landmine detection in thermal images: *a, b* – MOH-100 ma MOH-50 landmine in the grass; *c, d* – O3M-72 semiburied landmine; *e, f* – TM-62M buried landmine; the higher probability values are indicated by the from yellow to red palette; Legend: — – existing (detected) landmine, — – landmine detection failure

The performance of landmine detection was evaluated according to the following detection rates: the probability of correct landmine detection TP and the probability of false alarm FP :

$$TP = \frac{|M|}{|M_0|} \quad FP = \frac{|\bar{M}|}{|M| + |\bar{M}|} \quad (18)$$

where M_0 is the set of actual existing landmines, M is the set of correctly detected landmines, \bar{M} is the set of false detections; $|M|$ notation means the total number of elements in the set M .

The probability of correct landmine detection over test plots was 0.92, and the probability of false alarm was 0.45.

6 Discussion

The research outcomes show that the developed method provides a fairly high probability of correct landmine detection. This fact testifies the future prospects of one's application for the rapid obtaining of up-to-date maps of minefields.

At the same time, it should be highlighted that such a map cannot be the final document for decisions making on the threat presence/absence inside a minefield subplots, especially during the humanitarian demining, where according to the International Mine Action Standards (IMAS), it is required a 100 % mine detection probability [33, 34].

The obtained map can be used only as a geoinformation layer for further landmine clearance mission planning and determining the elements priorities within a minefield area. Although, of course, the availability of map with the localization of threatening subplots will significantly reduce both time and efforts for landmine clearance.

Unfortunately, the research has shown that the landmine detection false alarms frequency is also high. Even though this disadvantage does not pose an additional threat to life, it leads to deminer work complications.

The high frequency of false alarms can be understood as a payment for the fact that the method is based on the engagement of optical sensors only. Such sensors are not technically complex and costly. Known R&Ds (research and development) show that the incorporation of sensors operating in other spectral bands, in particular in the radio frequency bands, into the onboard set of sensors can reduce the number of false detections of landmines – see, for example [35]. However, due to the technical complexity of such sensors, their mass, and high power consumption, the requirements for the mobile platform (UAV) are essentially tightened, and the cost of the entire system increases significantly.

An improvement of the proposed method by developing the task-oriented database with spectral portraits of targets of interest and typical land covers can contribute to the efficiency enhancement of remote automated landmine detection.

7 Conclusions

The paper proposes a method for minefields mapping with the threatening subplots of terrain detection using aerial imaging from the UAV. To simplify the aerial imagers set, its operation and data processing, only optical images are used for landmine detection.

Algorithms for processing and classifying multispectral and thermal infrared images are developed. The method has been tested over sites with actual buried landmines.

Authors associate the method's future improvements with the GPR (ground penetrating radar) integration into the onboard aerial imagers set as well as with the artificial intelligence tools involvement for the aerial imagery analysis.

References

- [1] BALL, M. Landmine Detection with Drones. *Unmanned Systems Technology* [online], 2021, [viewed 2022-05-17]. Available from: <https://www.unmannedsystems.com/2021/08/landmine-detection-with-drones/>
- [2] *Detectors and Personal Protective Equipment Catalogue* [online]. Geneva: GICHD, 2009, [viewed 2022-05-17]. ISBN 978-2-940369-23-2. Available from: <https://www.files.ethz.ch/isn/97269/Metal-Detectors-Catalogue-2009.pdf>
- [3] EGE, Y., A. KAKILLI, O. KILIÇ, H. ÇALIK, H. ÇITAK, S. NAZLIBILEK and O. KALENDER. Performance Analysis of Techniques Used for Determining Land Mines. *International Journal of Geosciences*, 2014, **5**(10), pp. 1163-1189. DOI 10.4236/ijg.2014.510098.
- [4] MAATHUIS, B.H.P. Remote Sensing Based Detection of Minefields. *Geocarto International*, 2003, **18**(1), pp. 51-60. DOI 10.1080/10106040308542263.
- [5] *Acronyms and Slang* [online], 2022, [viewed 2022-05-17]. Available from: <http://acronymsandslang.com/definition/5267718/AMDAS-meaning.html>
- [6] GAUR, P. and T. CHOUDHARY. Aerial Landmine Detection. *International Journal of Engineering & Technology*, 2018, **7**(3.34), pp. 710-713. DOI 10.14419/ijet.v7i3.34.19457.
- [7] FARDOULIS, J., X. DEPREYTERE, P. GALLIEN, K. DJOUHRI, B. ABDOURHMANE and E. SAUVAGE. Proof: How Small Drones Can Find Buried Landmines in the Desert Using Airborne IR Thermography. *Journal of Conventional Weapons Destruction*, 2020, **24**(2), pp. 55-63. DOI 10.5281/zenodo.4409641.
- [8] RAJ, A., I. RAFIQ, A.J. GOWDA and L.S. KRISHNA. Landmines Detection Using UAV. *International Research Journal of Engineering and Technology* [online], 2019, **6**(4), pp. 2716-2719, [viewed 2022-05-17]. Available from: <https://www.irjet.net/archives/V6/i4/IRJET-V6I4577.pdf>
- [9] CASTIBLANCO, C., J. RODRIGUEZ, I. MONDRAGON, C. PARRA and J. COLORADO. Air Drones for Explosive Landmines Detection. In: ARMADA, M., A. SANFELIU and M. FERRE, eds. *ROBOT2013: First Iberian Robotics Conference. Advances in Intelligent Systems and Computing*. Cham: Springer, 2014, pp. 107-114. ISBN 978-3-319-03652-6.
- [10] COLOMINA, I. and P. MOLINA. Unmanned Aerial Systems for Photogrammetry and Remote Sensing: A Review. *ISPRS Journal of Photogrammetry and Remote Sensing*, 2014, **92**, pp. 79-97. DOI 10.1016/j.isprsjprs.2014.02.013.
- [11] RACEK, F., T. BALÁŽ T. and P. MELŠA. Hyperspectral Data Conversion in the Case of Military Surveillance. *Advances in Military Technology* [online], 2015, **10**(1), pp. 5-13, [viewed 2022-05-17]. Available from: <https://aimt.cz/index.php/aimt/article/1054>
- [12] XIANG, T.-Z., G.-S. XIA and L. ZHANG. Mini-Unmanned Aerial Vehicle-Based Remote Sensing: Techniques, Applications, and Prospects. *IEEE Geoscience and Remote Sensing Magazine*, 2019, **7**(3), pp. 29-63. DOI 10.1109/MGRS.2019.2918840.

- [13] POPOV, M.O., S.A. STANKEVICH, S.P. MOSOV, O.V. TITARENKO, M.V. TOPOLNYTSKYI and S.S. DUGIN. Landmine Detection with UAV-Based Optical Data Fusion. In: *IEEE EUROCON 2021 - 19th International Conference on Smart Technologies*. Lviv: IEEE, 2021, pp. 175-178. DOI 10.1109/EUROCON52738.2021.9535553.
- [14] LACROIX, V., Y. YVINEC and M. ACHEROY. Research at RMA in the Evolving Context of Mine Action. In: BEUMIER, C., D. CLOSSON, V. LACROIX, N. MILISAVLJEVIC and Y. YVINEC. *Mine Action – The Research Experience of the Royal Military Academy of Belgium*. London: IntechOpen, 2017, pp. 1-19. ISBN 978-953-51-3304-9.
- [15] LILLESAND, T.M., R.W. KIEFER and J.W. CHIPMAN. *Remote Sensing and Image Interpretation*. Hoboken: Wiley, 2015. ISBN 978-1-118-34328-9.
- [16] VENTURA, D., A. BONIFAZI, M.F. GRAVINA, A. BELLUSCIO and G. ARDIZZONE. Mapping and Classification of Ecologically Sensitive Marine Habitats Using Unmanned Aerial Vehicle (UAV) Imagery and Object-Based Image Analysis (OBIA). *Remote Sensing*, 2018, **10**(9), 1331. DOI 10.3390/rs10091331.
- [17] BUDIARTO, W., E. IRWANSYAH, J.S. SUROSO, A. CHOWANDA, H. NGARIANTO and A.A.S. GUNAWAN. Mapping and 3D Modelling Using Quadrotor Drone and GIS Software. *Journal of Big Data*, 2021, **8**, 48. DOI 10.1186/s40537-021-00436-8.
- [18] HOSMER Jr., D.W., S. LEMESHOW and R.X. STURDIVANT. *Applied Logistic Regression*. Hoboken: Wiley, 2013. ISBN 978-1-118-54838-8.
- [19] HILBE, J.M. *Practical Guide to Logistic Regression*. Boca Raton: CRC Press, 2015. ISBN 978-1-4987-0957-5.
- [20] KLEINBAUM, D.G. and M. KLEIN. *Logistic Regression: A Self-Learning Text*. New York: Springer, 2010. ISBN 978-1-4419-1741-1.
- [21] SINAGA, K.P. and M. YANG. Unsupervised k -Means Clustering Algorithm. *IEEE Access*, 2020, **8**, pp. 80716-80727. DOI 10.1109/ACCESS.2020.2988796.
- [22] STAROVOITOV, V.V. and Yu.I. GOLUB. Comparative Study of Quality Estimation of Binary Classification (in Russian). *Informatics*, 2020, **17**(1), pp. 87-101. DOI 10.37661/1816-0301-2020-17-1-87-101.
- [23] DAS, S.K. and R.S. SINGH. Performance Modelling of Electro-Optical Devices for Military Target Acquisition. *Defence Science Journal*, 2007, **57**(3), pp. 323-331. DOI 10.14429/dsj.57.1778.
- [24] TRUKHACHEV, A.A. *Analysis of Procedures and Algorithms for Signal Detection* (in Russian). Moscow: Radio & Communications, 2003.
- [25] HICKMAN, D.L. Target Detection: The Transition from Unresolved to Extended Targets. In: *Proceedings of the SPIE*, 2021, **11866**. DOI 10.1117/12.2597227.
- [26] CREMER, F., K. SCHUTTE, J.G.M. SCHAVEMAKER and E. DEN BREEJEN. A Comparison of Decision-Level Sensor-Fusion Methods for Anti-Personnel Landmine Detection. *Information Fusion*, 2001, **2**(3), pp. 187-208. DOI 10.1016/S1566-2535(01)00034-3.

- [27] DEN BREEJEN, E., K. SCHUTTE, and F. CREMER. Sensor Fusion for Anti-Personnel Landmine Detection: A Case Study. In: *Proceedings of Detection and Remediation Technologies for Mines and Minelike Targets IV*. Orlando: SPIE, 1999, **3710**, pp. 1235-1245. DOI 10.1117/12.357003.
- [28] KRTALIĆ, A., A.K. DIVJAK and R. ŽUPAN. Visualization of Land Mine Danger, Svilaja Region (Croatia). *Journal of Maps*, 2019, **15**(1), pp. 21-29. DOI 10.1080/17445647.2018.1552209.
- [29] KRTALIĆ, A. Thematic Maps for Humanitarian Demining. *Kartografija i Geoinformacije* [online], 2012, **11**(17), pp. 26-41, [viewed 2022-05-17]. Available from: <https://kig.kartografija.hr/kig/article/view/41>
- [30] SHAKHATREH, H., A.H. SAWALMEH, A. AL-FUQAHA, Z. DOU, E. ALMAITA, I. KHALIL, N.S. OTHMAN, A. KHREISHAH and M. GUIZANI. Unmanned Aerial Vehicles (UAVs): A Survey on Civil Applications and Key Research Challenges. *IEEE Access*, 2019, **7**, pp. 48572-48634. DOI 10.1109/ACCESS.2019.2909530.
- [31] PEPE, M., L. FREGONESE and M. SCAIONI. Planning Airborne Photogrammetry and Remote-Sensing Missions with Modern Platforms and Sensors. *European Journal of Remote Sensing*, 2018, **51**(1), pp. 412-436. DOI 10.1080/22797254.2018.1444945.
- [32] STANKEVICH, S.A., S.P. MOSOV and V.O. VOROVICH. Systematization of Conditions and Factors Influencing the Use of Drones in the Detection of Landmines (in Ukrainian). *Collection of the Scientific Papers of the Centre for Military and Strategic Studies of the National Defence University of Ukraine named after Ivan Cherniakhovskyi* [online], 2021, **3**(73), pp. 82-89. DOI 10.33099/2304-2745/2021-3-73/82-89. Available from: <http://znp-cvsvd.nuou.org.ua/article/view/255344/252428>.
- [33] MARQUES, L., G. MUSCATO, Y. YVINEC, M. PEICH, G. ALLI and G.A. TURNBULL. Sensors for Close-In Detection of Explosive Devices in the Framework of FP7-TIRAMISU Project. In: *The EOD Future in the Light of NATO EOD Demonstrations and Trials 2012*. Trenčín: NATO Centre of Excellence for Explosive Ordnance Disposal, 2013, pp. 63-74. ISBN 978-80-89261-42-0.
- [34] KRUIJFF, M., D. ERIKSSON, T. BOUVET, A. GRIFFITHS, M. CRAIG, H. SAHLI, F.V. GONZÁLEZ-ROSÓN, P. WILLEKENS and A. GINATI. Space Assets for Demining Assistance. *Acta Astronautica*, 2013, **83**, pp. 239-259. DOI 10.1016/j.actaastro.2012.08.016.
- [35] ZYADA, Z., Y. KAWAI, S. SATO, T. MATSUNO, Y. HASEGAWA and T. FUKUDA. GPR Environmental-Based Landmine Automatic Detection. In: HABIB M.K., ed. *Humanitarian Demining*. Vienna: IntechOpen, 2008, pp. 151-174. DOI 10.5772/5412.